Aerospace Science and Technology 105 (2020) 105982

Contents lists available at ScienceDirect

Aerospace Science and Technology

www.elsevier.com/locate/aescte

The role of shaft-speed oscillation on the instability behavior of transonic radial compressor

Hanxuan Zeng [a], Baotong Wang [b,*], Xinqian Zheng [a,b]

[a] Turbomachinery Laboratory, State Key Laboratory of Automotive Safety and Energy, Tsinghua University, Beijing, 100084, China
[b] Department of Aerodynamics and Thermodynamics, Institute for Aero Engine, Tsinghua University, Beijing, 100084, China

ARTICLE INFO

Article history:
Received 31 March 2019
Received in revised form 28 April 2020
Accepted 28 April 2020
Available online 16 June 2020
Communicated by Kivanc Ekici

Keywords:
Compressor
Free-spool
Surge dynamics and limit
Dynamic simulation
Experimental investigation

ABSTRACT

A dynamic model of the free-spool compression system is established to investigate the effects of rotational speeds oscillation on the surge characteristics and behaviors. Simulation results show better agreement with the experimental data compared to the fixed-spool simulation, which confirms the importance of introducing rotor dynamics into surge modeling. The mechanism of the prolonged surge cycle is presented, as well as an overall comparison and explanation of discrepancies in surge characteristics between different operating speeds and design cases. It is pointed out that the relative position of the averaged deceleration line and the surge line is critical in leading to the discrepancies. Further perturbation analysis concerning the effects on the surge limit suggests that reducing the rotational inertia of the spool may enhance the system stability under certain circumstances, which can be evaluated by the speed variation contribution parameter (SVC). The results may further contribute to the design of surge control system.

1. Introduction

Compressors are widely used in aero-engines and industrial gas-turbines to provide highly compressed air for combustion and energy extraction process. However, the reliability and safety of this kind of power plant are strictly limited by the stable operating range of compressor. The operable range of compressor is constrained between the choked mass flow rate and the unstable mass flow rate. The later one is commonly referred to the surge line. Surge causes significant drop in compressor pressure-rise and vibration in engine components [1]. The transient axial force due to surge with large magnitudes severely damages the bearings and the shafting system [2–4]. Therefore, compressor surge needs to be strictly controlled during design and usage.

Surge was studied extensively over the past few decades [5–7]. The first identification of compressor surge dates back to 1950s. At that time, lacking of detailed experimental measurements limited the description of surge to acoustic and vibration issues [8,9]. Thorough measurements on different types of compressors later on pointed out the systematic instability and backflow features of surge [10]. It is common to distinguish surge between two different patterns: mild surge and deep surge. The former type of surge features frequency similar to the system Helmholtz frequency [11,12], and the amplitude is relatively low, while the frequency of deep surge is well below the Helmholtz frequency [13] since it is decided by the period to fill and empty the downstream plenum. Day further pointed out that the two surge patterns are related to the shape of compressor characteristic curve [14]. In addition, it is important to distinguish surge from rotating stall for their different effects on the compressor behavior. The B-parameter proposed by Greitzer [10] is one of the most noted example, which became a popular topic in this field for studying the surge characteristic. Based on this, more parameters representing the compressor design features were introduced to predict the critical B-parameter more accurately [14]. Additionally, the operating conditions was also found to have effects on the surge characteristics, and a good example is that the surge frequency decreases slightly with increasing rotational speed [15].

Based on the past analytical and experimental works, we find out that surge features systematic instability and different patterns. However, for aero-engines and gas turbine engines, the compressor is driven by the downstream turbine by direct connection. Therefore, the variation of power consumption caused by the compressor surge would result in the imbalance of power between the compressor and turbine, then the shaft speed will oscillate. Traditionally this dynamic effect was neglected when modeling

* Corresponding author.
E-mail address: wangbaotong@tsinghua.edu.cn (B. Wang).

https://doi.org/10.1016/j.ast.2020.105982
1270-9638/

Nomenclature

A	area
A_s	inertia parameter $\frac{2\rho LAr_t^2}{I}$
B	system parameter, Equation (7)
C'	slope of the compressor pressure-rise characteristics
I	moment of inertia
k	gas constant
L	pipe length
N	shaft rotational speed
T'	slope of the valve characteristics
V	plenum volume
Π	pressure ratio
Ω	shaft angular velocity
Γ	torque parameter $\frac{\tau}{\rho Ar_t U^2}$
λ, Ψ	total to static work coefficient $\frac{c_p T_{t1}(\pi^{\frac{\gamma-1}{\gamma}}-1)}{U_2^2}$
φ, Φ	flow coefficient $\frac{m}{4\rho_{t1}U_2 r_2^2}$
τ	torque, non-dimensional time

Subscripts

c	compressor
d	turbine
p	plenum
s	shaft
t	impeller tip & throttle
cor	corrected with standard condition
sur	surge
chk	choke
1	impeller inlet
2	impeller outlet
3	diffuser inlet
4	diffuser outlet
nor	normalized by the choked condition

the entire compression system, such as the models established by Greitzer [16,10] and Moore and Greitzer [17,18], by which primary features of surge and rotating stall were captured. Mansoux et al. [19] developed a distributed non-linear model that is suitable for control system design. Righi et al. [20] combined the conventional body-force model with a zero-dimensional piping system model, which is capable of modeling the complete surge cycle. Zhang et al. [21] developed a one-dimensional and three-dimensional coupled method to predict the surge boundary. Despite that main features of surge are captured by these models, some detailed surge behaviors are hard to reproduce, such as the non-periodic phenomenon. The spool inertia was modeled and analyzed first by Fink et al. [22], and the time-resolved results show considerable increase in time interval between surge blowdowns. Also, this speed effects magnify with decreased spool inertia. The result stresses the importance in modeling the rotor dynamics. The model with spool inertia was applied and further validated by Abrassi et al. [23] and Gravdahl et al. [24], and the simulation results agree well with transient experimental results at some operating speeds. Recently, Zheng et al. [25] tested a small radial compressor at full operating range with dynamic signals of compressor outlet pressure measured during surge. According to the results, the non-periodic surge phenomenon was also found, however this shaft-speed-oscillation-induced phenomenon behaves inconsistently at different operating speeds. At some speeds, it is insensitive to the speed transient which implies that there are other factors affecting this non-periodic phenomenon. As the characteristics of surge are critical in evaluating the potential damage to the machine [4], it is essential to further investigate this topic.

The purpose of this paper is to investigate the effects of spool speed variation on the surge dynamics with special emphasis on the foresaid problems. This paper consists of three sections: (1) A free-spool compressor system model is established based on two transonic radial compressors. (2) The effects of speed variation on surge dynamics are discussed based on the simulation and experimental results. (3) The effects of speed variation on surge limit are discussed based on the perturbation analysis.

2. System dynamic model

In this section, an analytical methodology to build a dynamic model of free-spool compression system is presented. A description of the dynamic model is given first to include the governing equation over compression and shafting systems. Detailed compressor modeling method and results are given after that.

2.1. Governing equation

The system dynamic model is established based on the works by Greitzer [16] and Fink et al. [22]. To simulate the surge dynamics at different operating speeds, as well as to take the shape of the compressor surge line into consideration, dimensional form of governing equations are necessary to perform the calculations. Detailed derivation of the following equations is omitted for brevity, yet readers can find it in the references mentioned above.

A classic compression system configuration is adopted here consisting of a compressor, downstream pipe and plenum, as well as a throttle. Compressor characteristics are modeled using a built-in performance map based on the experimental data, which will be discussed in the following section. The flow in downstream compressor pipe is regarded to be incompressible and modeled with one-dimensional momentum equation as

$$\frac{L_c}{A_c}\frac{d}{dt}(\dot{m}_c) = P_c - P_p \tag{1}$$

where L and A are reference length and area of the downstream plenum-throttle system respectively. The continuity equation along with the hypothesis of isentropic compression process is employed to the plenum V as

$$\frac{d}{dt}(\rho_p V_p) = \dot{m}_c - \dot{m}_t \tag{2}$$

in which ρ is the plenum density, and $\dot{m}_c$ and $\dot{m}_t$ are the compressor and the throttle mass flow rates. $\dot{m}_t$ is further calculated through throttle equation as

$$\dot{m}_t = \sqrt{(P_p - P_{ref})/K_t} \tag{3}$$

To include rotor dynamics into the model, the rate of speed change is decided by the shaft torque of compressor and turbine respectively as denoted by τ_c and τ_d

$$I\frac{d\Omega}{dt} = \tau_d - \tau_c \tag{4}$$

Substituting τ with shaft work, Equation (4) is rearranged as follows

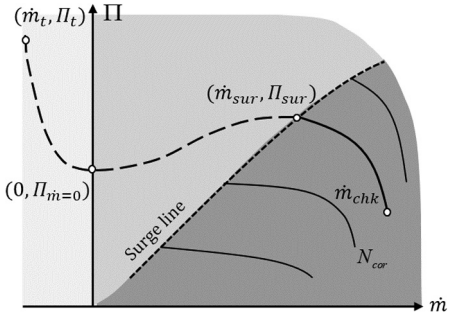

Fig. 1. Sketch of the complete compressor map.

$$I\frac{dN}{dt} = (\frac{60}{2\pi})^2 \frac{1}{N}(Power_d - Power_c) \tag{5}$$

In Equation (5) the turbine power $Power_d$ is almost constant because of the cavity effects of the combustor while $Power_c$ is updated at every time step. The governing equations (1) (2) (3) (5) are adequate in describing this dynamic system. They are solved using explicit Fourth-Order Runge-Kutta method combined with compressor map generated in the next section. The time step size is set to 5e-5, which is well below the Helmholtz frequency (around 10 Hz) so that the sufficient time-resolution is guaranteed.

2.2. Compressor modeling

In this section, the compressor map is fitted to a segmented function with intervals defined according to the steady and transient experimental data. A typical compressor map is shown in Fig. 1, in which different gray scale regions represent different fitting functions applied to ensure adequate precision. The location of surge line (dotted line), as well as the stable operating range on its right-hand side, indicated by the solid black line, are fitted based on the steady experimental results. As for the left branch of the compressor characteristics, dynamic experimental data are used to calibrate the function coefficients and validate the simulation results instead of defining the location directly for the extreme difficulties in tracking the highly transient compressor behavior during surge cycles. The hysteresis due to compressibility is normally modeled by a time constant that is not significant in our tested cases. The method suggested below provides simple but accurate enough results.

In general, for each constant rotational speed, the performance curve is divided into three sub-intervals ($\dot{m} < 0, 0 < \dot{m} < \dot{m}_{sur}, \dot{m}_{sur} < \dot{m} < \dot{m}_{chk}$). A third-order polynomial fitting is employed if $0 < \dot{m} < \dot{m}_{sur}$ and the local slope at the zero mass flow point is set to zero [17] [26]. This function is defined in a way that the location of the compressor surge line is constrained to the experimental results as well as its local slope. This is critical because the surge dynamic is investigated around this region. Also, the magnitude of pressure fluctuation during surge is highly dependent on point $(0, \hat{\Pi}_{\dot{m}=0})$ so that $\hat{\Pi}_{\dot{m}=0}$ is set to be the lowest pressure during surge based on the time-resolved experimental data at the compressor outlet [27]. A non-elementary function is utilized for $\dot{m}_{sur} < \dot{m} < \dot{m}_{chk}$ to capture both the unimodal and choked compressor characteristics. For $\dot{m} < 0$, the performance curve is modeled with a turbine like behavior [27]. This function shows good flexibility for model tuning to fit the transient experimental results in negative flow range. A collection of equations is shown in Equation (6).

$$\begin{cases} \hat{\Pi} = (-a_1^2\dot{m}^2 + a_2\dot{m} + a_3) \cdot (\dfrac{a_4}{\dot{m} - \dot{m}_{chk}} + 1) & \dot{m}_{sur} < \dot{m} < \dot{m}_{chk} \\ \hat{\Pi} = -b_1\dot{m}^3 + b_2\dot{m}^2 + a_3\dot{m} + a_4 & 0 < \dot{m} < \dot{m}_{sur} \\ \hat{\Pi} = \hat{\Pi}_{\dot{m}=0} + (1 - (\dfrac{\dot{m}}{k_1})^2)^{-1/k_2} & \dot{m} < 0 \end{cases} \tag{6}$$

The parameters in Equation (6) are determined using the nonlinear least square method based on the experimental data in tested speeds, and they are interpolated to the untested speeds. Usage of different interpolating functions is somewhat empirical, for example, the local slope variation at near surge point is linearly fitted to the experimental data and shows good consistency. Compressor power characteristics are modeled in the same manner with pressure ratio, and the linear fitting also shows good agreement. An overview of the fitted compressor map is sketched in Fig. 2 along with experimental data marked by spots.

In fact, several studies have pursued further to obtain the compressor characteristics by experiments past the compressor surge line. Fink et al. [22] extended the speed lines clearly to near shut-off with a close coupled valve installed just downstream of the compressor volute exit. Hansen et al. [11] managed to measure the negative branch of the steady-state characteristic by feeding air to the compressor exit to force a steady negative flow. Both of the methods are feasible but going to be a long haul to complete. In this paper, a simple method is presented, which can simulate surge dynamics with adequate precision as will be shown in the next section.

3. Surge characteristics and behavior

In this section, simulations are conducted at the surge point. Dynamic pressure results are compared with the experimental data to highlight the differences introduced by the rotor dynamics. Simulations are also conducted at different rotational speeds, followed by a general explanation of how the rotor dynamics influence the compressor surge.

3.1. Experimental setup and results

Two different radial compressors are machined and tested (named $C1$ and $C2$ respectively). The two cases are selected to represent both low and relatively high design total pressure ratio equal to 3.6 (compressor $C1$) and 5.6 (compressor $C2$). Besides, compressor $C2$ is designed with a vaneless diffuser which makes the compressor characteristics flatter at low speeds. This feature is shown to be responsible for the inconsistency of surge dynamics between different operating speeds later.

The test rig extracts energy from the combusted air through a power turbine to maintain the power balance. Fuel supplied to the combustor is regulated by a close-looped control system while leaving the speed control to be open-looped. The power turbine and the tested compressor are mounted on the same shaft as shown in Fig. 3. Low-frequency-response probes are mounted both upstream and downstream of the tested compressor to obtain the overall total-to-total performance characteristics. Transient pressure signals inside the compressor are captured by sixteen high response pressure transducers (*Kulite* XTE-140(M) [28]). A standard miniature silicon diaphragm is used to reach extremely high natural frequencies in the smallest thread mount available. The natural frequency varies from 240 kHz (pressure range of 25 psi) to 380 kHz (pressure range of 100 psi) depending on the local pressure. Besides, a protective grid is used in each probe to ensure the reliability of the sensing part.

The two investigated compressors are transonic designs. In addition to the compressor component, its upstream and downstream pipe installation extends far away from the inlet and the

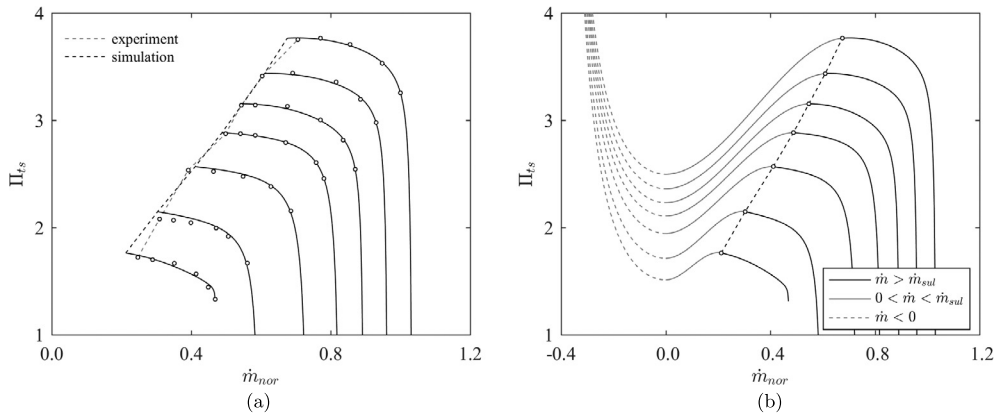

Fig. 2. (a) Fitted results compared with steady experimental data, (b) Overall compressor map modeling results.

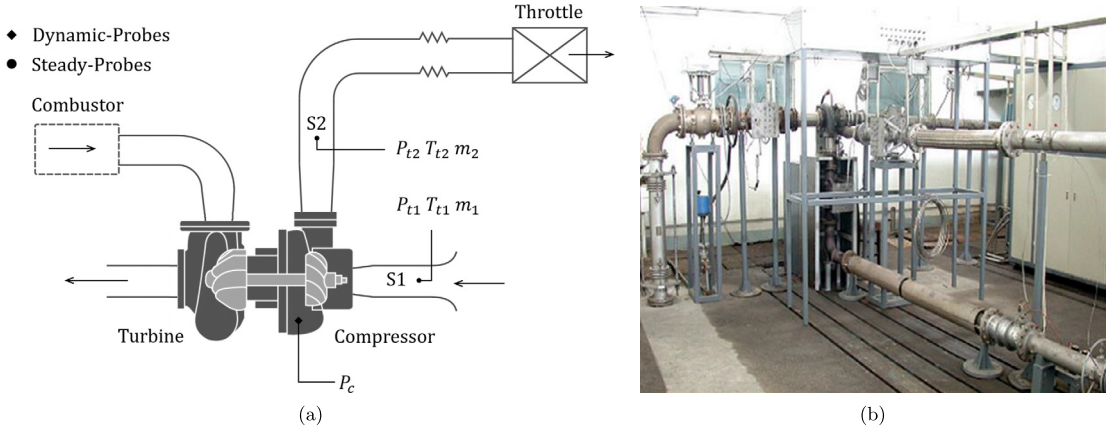

Fig. 3. Test facility: (a) sketch of the main test facility, (b) overview of the test-rig.

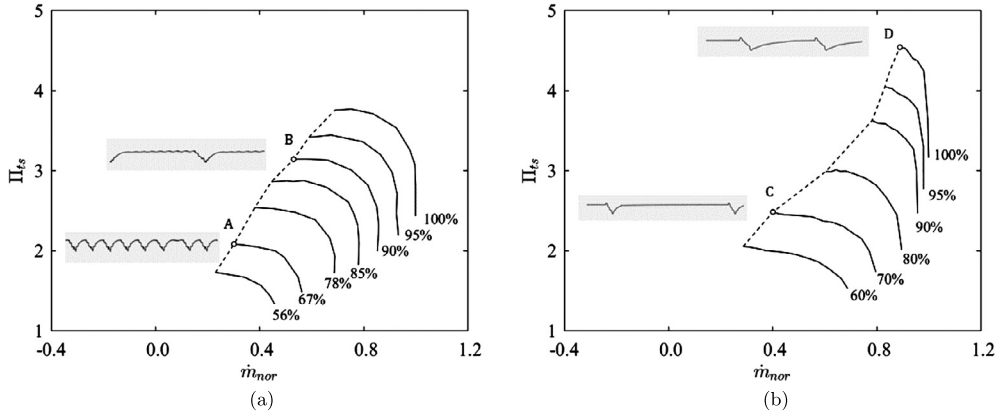

Fig. 4. Performance characteristics of the tested compressors: (a) compressor $C1$, (b) compressor $C2$.

outlet. This system configuration has great effects on the surge and stall characteristics. However, no evident plenum is attached to the compressor outlet. Therefore, the compression system cannot be directly applied to the calculation of B-parameter. In order to find the B-parameter for analyzing the dynamic behaviors, the natural frequency is estimated by the mild surge frequency captured by high response pressure transducers at the middle-speed range as shown in Fig. 4. Because the mild surge frequency is proved to be quite close to the Helmholtz-frequency [25] [29], the B-parameter is calculated for both test cases with Helmholtz-frequency by Equation (7)

$$B = \frac{U}{4\pi f_H L} \tag{7}$$

In Equation (7) the Helmholtz frequency f_H is around 10 Hz for both cases. The detailed compressor and system configuration can be found in Table 1.

The obtained steady and transient experimental results are combined to provide an overview of the performance characteristics of the two tested compressors as shown in Fig. 4. The transient pressure signals at surge points are measured by closing the downstream valve until noticeable fluctuation is observed (Point A to D). Deep surge cycles are clearly shown at each point, and the period of surge cycles varies significantly between different speeds. Although the increased rotational speed has already been found to be responsible for the prolonged surge cycles [24], the contribution is way less than the magnitude observed in this experiment.

Table 1
Specification of the test compressors $C1$ and $C2$.

Parameters	Symbols	$C1$	$C2$
Impeller blade number	Z_I	16	24
Leading edge tip radius	r_{1t}/r_2	0.63	0.65
Diffuser vane number	Z_D	16	0
Diffuser inlet radius	r_3/r_2	1.18	1.10
Diffuser outlet radius	r_4/r_2	1.44	1.48
Impeller tip Mach number	M_u	1.4	1.8
Flow coefficient	φ	0.04	0.06
Work coefficient	λ_{tt}	0.47	0.75
Specific speed	N_s	0.7	0.61
System parameter	B	1.22	2.00

By considering the lumped-parameter model of the compression system, the contribution is roughly estimated by using the non-dimensionalized time as Equation (8).

$$\tau = \frac{1}{\omega_H} = a\sqrt{\frac{A}{LV}} \tag{8}$$

In Equation (8), a is the plenum sonic velocity that is proportional to the operating speed. Other parameters are constant and determined by the compression system geometry. It is calculated that τ increases by about 16% from point A to point B, which is unable to fully account for the significant decrease of surge frequency shown in Fig. 4. Furthermore, comparing point C with point D, the surge frequency is even larger at the higher rotational speed, which is completely contradictive with the calculation above. Additionally, it can be seen that, within the prolonged surge cycles at point B and C, fluctuations featuring Helmholtz-frequency exist. This is commonly induced by the switching between mild surge and deep surge. However, this phenomenon vanishes at other speeds.

Past works showed the relation between the spool speed oscillation with this switching phenomenon, but it fails to explain the inconsistency between operating speeds as discussed above. Therefore, a more comprehensive study is needed to identify how merging phenomenon happens and its interaction with different operating speeds, which will be presented in the following sections.

3.2. Influences on surge characteristics at single operating speed

Simulation is conducted with and without speed variation involved at 90% design speed based on the parameters specified in Table 1 of compressor $C1$.

The moment of inertia I_0 is calculated from CAD models, and the material properties are those used during the test. To minimize systematic errors from manufacture and assembly, as well as to cover possible shafting configurations of analogous test-rig, the moment of inertia varies under reasonable range. The experimental and simulated results are combined to show the effects of bringing in the rotor dynamics in Fig. 5. It can be seen that the first few surge cycles have roughly the same frequency. Then, the experimental and free-spool simulation results show a significantly longer time of pressure recovery period, while the fixed-spool system continues to surge in a constant frequency. After the 3000th impeller revolution, the quiet period is no longer sustainable and breaks down again. It is clear that the free-spool simulation agrees better with the experimental data. Besides, the time series of spool rotational speed indicates that the compressor speed deceleration due to pressure breakdown is responsible for the prolonged surge cycle.

Additional simulations are conducted with the spool rotational inertia equal to $0.8I_0$ and $2.0I_0$ to investigate the significance of this dynamic effect. For the case with reduced rotational inertia

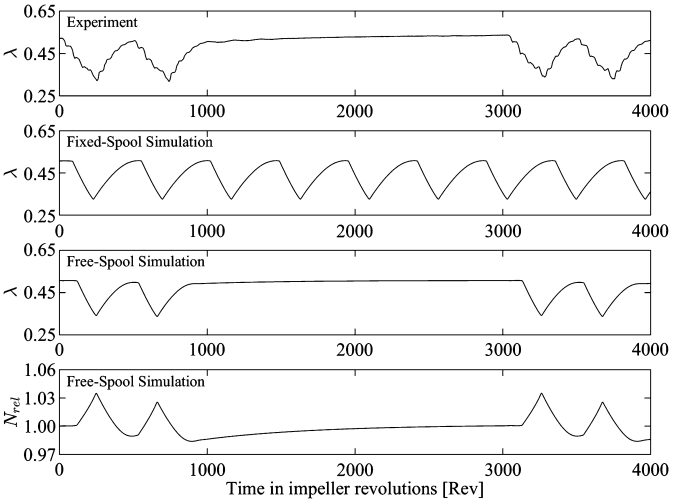

Fig. 5. Work coefficient comparison of experimental data and simulated results at 90% design speed of compressor $C1$ (free-spool simulation is conducted with rotational inertia of I_0).

as shown in Fig. 6a, the quiet period has shortened from 1.3 s to 0.4 s due to a more rapid response of the system. Besides, small pressure fluctuations are observed at this period featuring the magnitude of Helmholtz frequency (*phase*_2). Turning to the other case with $2.0I_0$ shown in Fig. 6b, doubled rotational inertia eliminates the quiet period. Also, the magnitude of spool rotational speed variation is less significant, but still oscillates as the surge cycles proceed. The averaged rotational speed increases at the start of surge and then decreases gradually until a periodic state with averaged rotor speed is reached after the 1400th impeller revolution. Comparing the two simulations, it can be concluded that the rotor dynamics have essential effects on surge characteristics, especially the existence of the quiet period.

From Fig. 7, details are presented concerning how the speed variation triggers the quiet period during surge. Point A, A', B and C also correspond to those in Fig. 6. At *phase*_1, the compressor enters into surge with the throttle slightly closed at the surge limit position (point A). The shaft speed increases soon after surge happens until pressure recovery process begins, and the compressor mass flow rate reaches its maximum. After that, the compressor operates under choke conditions, where the compressor power consumption is quite high. Hence a much significant deceleration process drives the system operating at an even lower rotational speed near the surge line (point B) comparing to the surge initial state. Therefore, a quasi-steady state can be reached after one or several surge cycles when the operating point is away enough from the surge line (*phase*_2). During this period, since the compressor power consumption is much lower than that at the beginning, the shaft would re-accelerate until a new surge limit (point C) is reached, which brings the compressor into surge again (*phase*_3).

An averaged deceleration line is sketched in Fig. 7 from A' to B. If the throttle position is fixed, this line would be closely fitted to the valve characteristics. Additionally, due to the quasi-steady state of *phase*_2, the compressor would also accelerate along line $A'B$. It is clear from the sketch that the surge pattern changes (or quiet period appears) as long as the deceleration effect is significant enough.

It is noticed from the simulation results that the transient operating point crosses the surge line at some rotational speeds during *phase*_2, but the system still operates well without entering into deep surge. This stabilizing effects during transients are discussed more in details in the following sections using perturbation method. Moreover, the existence of *phase*_2 and *phase*_3 mainly results from the energy imbalance of the shaft. Therefore, accurate

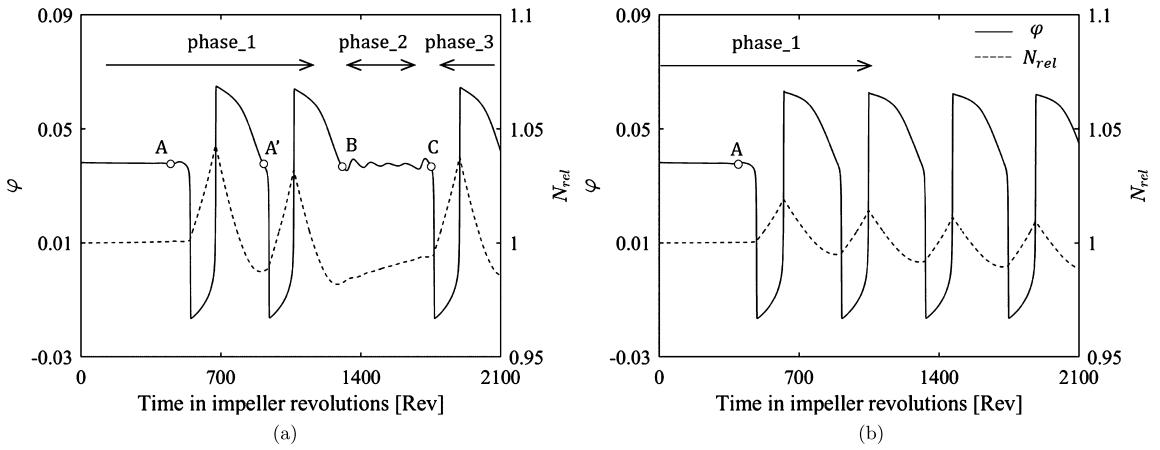

Fig. 6. Time history of flow coefficient and spool rotational speed at 90% design speed: (a) rotational inertia of $0.8I_0$, (b) rotational inertia of $2.0I_0$.

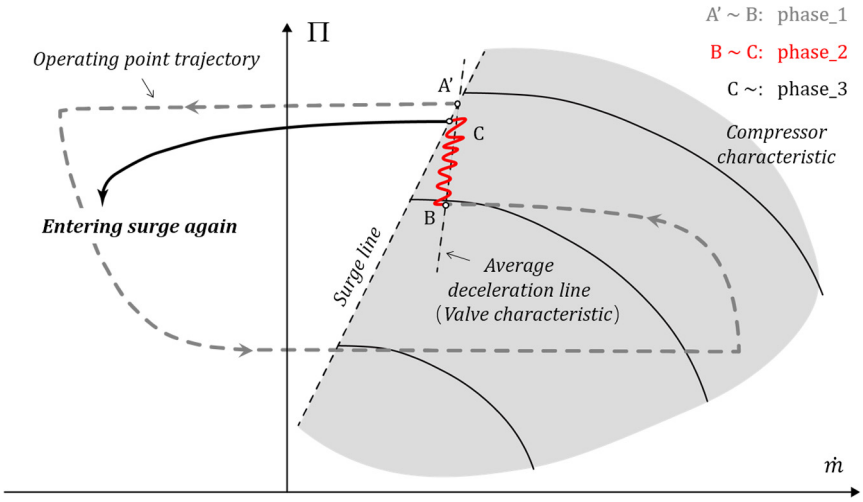

Fig. 7. Sketch and explanation of the prolonged surge cycle. (Rotational inertia of $0.8I_0$.)

adjustment of the energy balance at the end of *phase*_1 may provide an effective way of surge prevention without sacrificing the engine performance much.

3.3. Influences on surge characteristics between different operating speeds

When the surge characteristics at different operating conditions are considered, it is apparent that the duration of a single surge cycle is changing with operating speed lines and design cases. Fig. 8 presents the experimental data of pressure signals at the entire speed range. For compressor $C1$, a comparison of time series *d* and *e* shows that the surge frequency reduces from 4 Hz to 3.3 Hz with increased rotational speed from 56% to 67% design speed. This frequency reduction results from the increased B-parameter as mentioned earlier. With the rotational speed is further increased, the merging phenomenon appears and dramatically prolongs the time of surge cycles. The quiet period continues to extend until the design rotational speed is reached, and the surge frequency is reduced to nearly 1 Hz. Contrary to compressor $C1$, the quiet period appears at lower operating speeds for compressor $C2$. This inconsistent surge dynamics indicate that the effects of spool speed variation are strongly dependent on the operating conditions and design features.

It has been noted that the slope of the averaged deceleration line dominates the behavior of compressor surge with variable spool speed. Also, the location of surge boundary varies at different operating speeds for each design case. To deal with this problem, two simulations have therefore been done by adjusting the valve characteristics to change the relative position between the valve characteristic curve and the compressor surge line. Results are shown in Fig. 9. For both cases, the modeled compression system is identical except the slopes of the downstream valve characteristic curve. For case II with smaller slope of valve characteristics, deep surge cycles grow continuously, and the quiet period vanishes due to closely matched surge line. This result corresponds to the experimental data at lower speeds of compressor $C1$ and higher speeds of compressor $C2$. For case I, the quiet period appears with an increased slope of the valve characteristic curve. Therefore, although the averaged deceleration line dominates the merging phenomenon, it can be concluded that deep surge would still be stable if the local slope of the surge line is larger than or close to the valve characteristics.

In support of the simulation results, different designs of compressor indeed exhibit the possibility of this inconsistency in the change of surge dynamics with rotational speed. Typically, the compressor surge line is non-linear, especially for transonic compressors, in which operations at high-speed range suffers greatly from the flow separation induced by the shock wave. As a result, stall cells grow rapidly and extend to the whole passage that finally develop into surge. Because of this, the surge line tends to be much steeper at higher speeds. Besides, the surge lines of compressors with different design pressure ratio and flow capacity

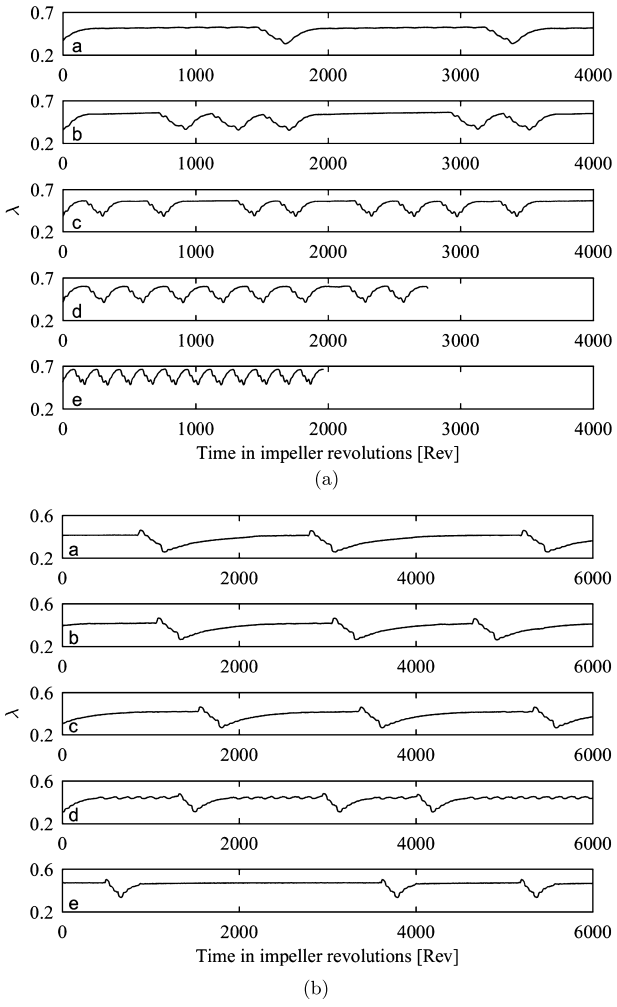

Fig. 8. Comparison of surge characteristics at different rotational speeds, experimental results: (a) compressor $C1$, from a to e: 90%, 85%, 78%, 67%, 56%; (b) compressor $C2$, from a to e: 100%, 97%, 95%, 80%, 70%.

naturally intersect with the valve characteristic curve in different ways.

To further prove the presented explanation, the characteristic curves of four different opening positions of the downstream valve are sketched in Fig. 10 in combination with performance maps of the two tested cases. The valve is modeled using a parabolic function defined by a fixed point that the pressure ratio equals to one when the compressor is completely throttled. $Valve\_1$ and $Valve\_2$ intersect with the surge line of compressor $C1$ at the speed of 56% and 90% as denoted by A and C. $Valve\_3$ and $Valve\_4$ intersect with the surge boundary of compressor $C2$ at the speed of 60% and higher speed lines as denoted by B, D and E. $Valve\_1$ nearly overlaps with the surge line of compressor $C1$ near the intersection point A, while the local slope of $Valve\_3$ is clearly greater than the surge line of compressor $C2$ near the intersection point B. Consequently, the merging phenomenon happens more frequently at low-speed range of compressor $C2$ instead of compressor $C1$, which coincides with the experimental results showed in Fig. 8. Analogously, operating point C is subject to the switching of surge patterns, but D, E are more insensitive to it because of a marked increase in the slope of the surge line at higher rotational speeds.

One last point should be mentioned here is that the inconsistent features of surge dynamics are modeled by the system simulation. However, it is not available if simulations are conducted based on the lumped-parameter models in which one single curve is used to represent the whole performance map. This is because the non-linear feature of the surge line is dropped. Also, for radial compressors with vaned diffuser, the performance curves would not collapse into a single curve due to the shifting of throat from impeller to diffuser at different rotational speeds. For this reason, complete modeling of compressor map is recommended to capture more information, especially at near surge regions.

4. Surge limit and control

In previous sections, the effects of variable rotational speed on the surge characteristics and behaviors are investigated. It is noted that the operating point oscillates outside of the surge line at *phase*_2 at some rotational speeds, but the system still operates well without surge, which indicates a stabilizing effect during variable speed operation. Therefore, further simulations are conducted at surge initial phase with different rotational inertia to study this effect. Time histories of the mass flow rate are combined and shown in Fig. 11. With a smaller rotational inertia of $0.2I_0$ represented by the solid dark curve (*case*_1), the pressure fluctuation induced by throttling is stabilized to a new equilibrium state, while the case with a larger moment of inertia equal to $2I_0$ falls into surge eventually as indicated by the dashed curve (*case*_3). Comparison of the two results confirms the stabilizing effect introduced by rotor dynamics. However, when the valve is further throttled slightly from 0.359 to 0.358 (*case*_2), the compressor goes into surge in the end. Even though the extended stable range is not significant in this case, study on the potential of reducing the shaft inertia still provides us a future direction for compressor instability control.

Further analysis is done base on a lumped-parameter model [22]. This nondimensional model takes rotor dynamics into consideration and is simplified to the degree so that the main features of the system can still be captured according to the results. The perturbation method is applied to investigate how the stable operating range of this non-linear system changes with the spool speed variation, and also its sensitivity to the system parameters is discussed.

The model is summarized and rearranged as the equations listed below:

$$\begin{cases} \dfrac{dB}{dt} = -\dfrac{1}{2\Psi_p}\dfrac{k-1}{k}(\Phi_c - \Phi_t) + A_s B^2(\Gamma_d - \Gamma_c) \\ \dfrac{d\Psi_p}{dt} = \dfrac{1}{B}(\Phi_c - \Phi_t) + 2A_s B\Psi_p(\Gamma_c - \Gamma_d) \\ \dfrac{d\Phi_c}{dt} = B(\Psi_c - \Psi_p) + A_s B\Phi_c(\Gamma_c - \Gamma_d) \end{cases} \tag{9}$$

The above three equations are derived according to the balance of shaft torque, as well as the conservation of momentum and mass flow rate (part of the derivation is found in Appendix A). Parameter B accounts for the spool rotational speed and plenum temperature variation as expressed by $B = f(T_p, U)$. Equation (9) is linearized, and the stability analysis based on the derived perturbation equation (10) can be conducted.

$$\frac{d}{dt}\begin{bmatrix} \delta\Phi_c \\ \delta\Psi_p \\ \delta B \end{bmatrix} = \begin{bmatrix} \overline{B}C' + A_s\overline{B}\Gamma_c'\overline{\Phi}_c & -\overline{B} & -A_s\overline{B}\Gamma_d'\overline{\Phi}_c \\ \frac{1}{\overline{B}} + 2A_s\overline{B}\Gamma_d'\overline{\Psi}_p & -\frac{1}{\overline{B}T'} & -2A_s\overline{B}\Gamma_d'\overline{\Psi}_p \\ -\frac{k-1}{2k}\frac{1}{\overline{\Psi}_p} - A_s\overline{B}^2\Gamma_c' & -\frac{k-1}{2k}\frac{1}{\overline{\Psi}_p} & A_s\overline{B}^2\Gamma_d' \end{bmatrix}\begin{bmatrix} \delta\Phi_c \\ \delta\Psi_p \\ \delta B \end{bmatrix} \tag{10}$$

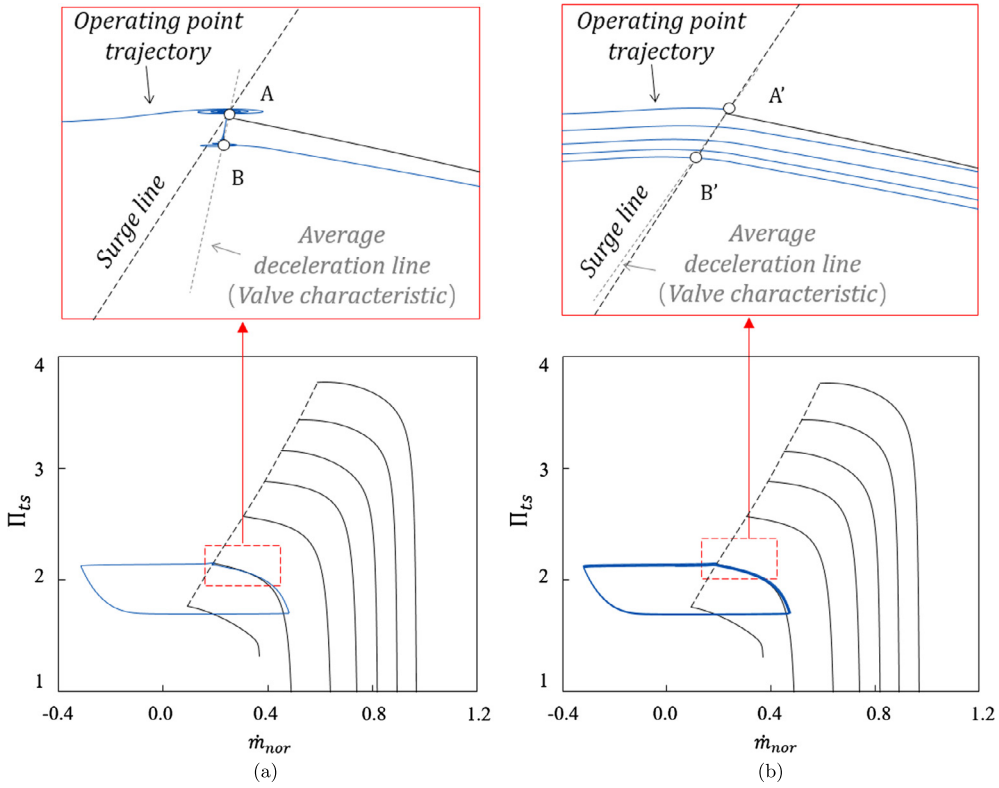

Fig. 9. Simulation results of different relative position of the valve characteristic curve and the compressor surge line, (a) case I: simulation with larger slope of valve characteristic; (b) case II: simulation with smaller slope of valve characteristic.

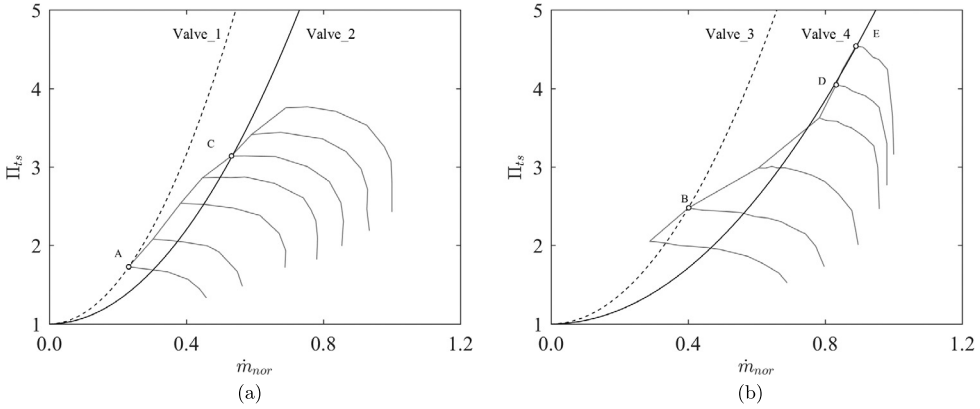

Fig. 10. Performance map of tested compressors combined the valve characteristics: (a) compressor $C1$, (b) compressor $C2$.

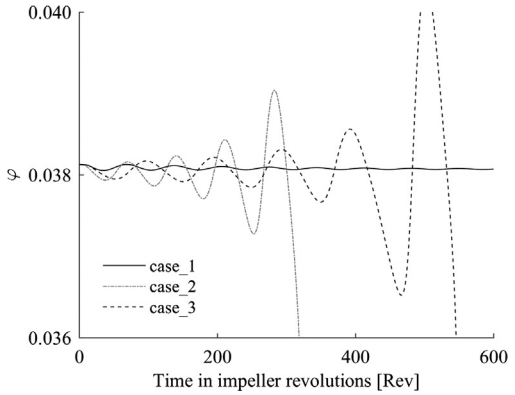

Fig. 11. Stabilizing effect of variable rotational speed (*case*_1: $0.2I_0$, $A_t = 0.359$; *case*_2: $0.2I_0$, $A_t = 0.358$; *case*_3: $2.0I_0$, $A_t = 0.359$).

The fixed-spool model is easily obtained by setting the nondimensional parameter A_s to zero representing infinite rotational inertia. For brevity, the fixed speed model is denoted by G_{model}, while the variable speed model is denoted by F_{model}. According to the Routh Criterion, four stability conditions are derived for the F_{model} denoted by $Cond1$ to $Cond4$, as well as two well-established conditions for the G_{model}. The detailed derivation and expression of those conditions can be found in Appendix B. These conditions should be satisfied (positive) at the same time to ensure the stability of the entire compression system for each model. The stable regions of each condition for both models with respect to the local slope of the compressor and valve characteristic curve (denoted by C' or $T' = d\Psi/d\Phi$) at the near surge point are shown in Fig. 12, and the dark gray region in each figure represents the stable region satisfying both conditions. In this analysis, parameter A_s is set to 0.05 for the variable speed calculation to ensure that the spool speed changes within a normal range in practical usage. Moreover,

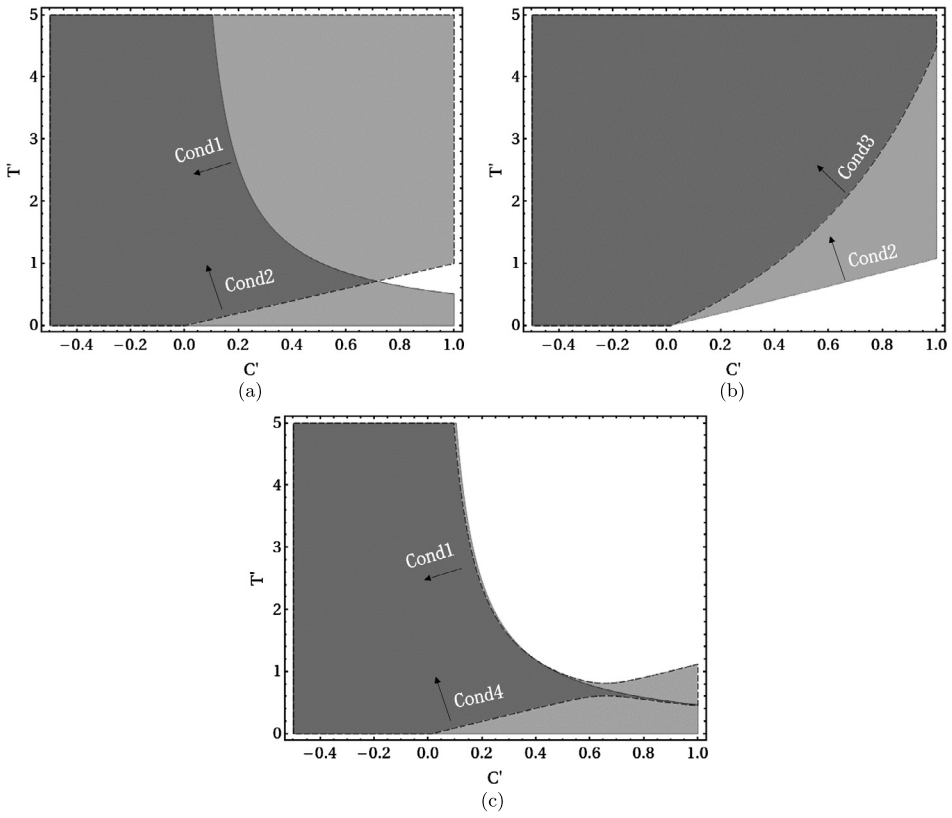

Fig. 12. Stability region with respect to the slope of compressor (C') and valve (T') characteristic: (a) Fixed spool system model (G_{model}, $A_s = 0$), (b)(c) Variable speed system model (F_{model}, $A_s = 0.05$).

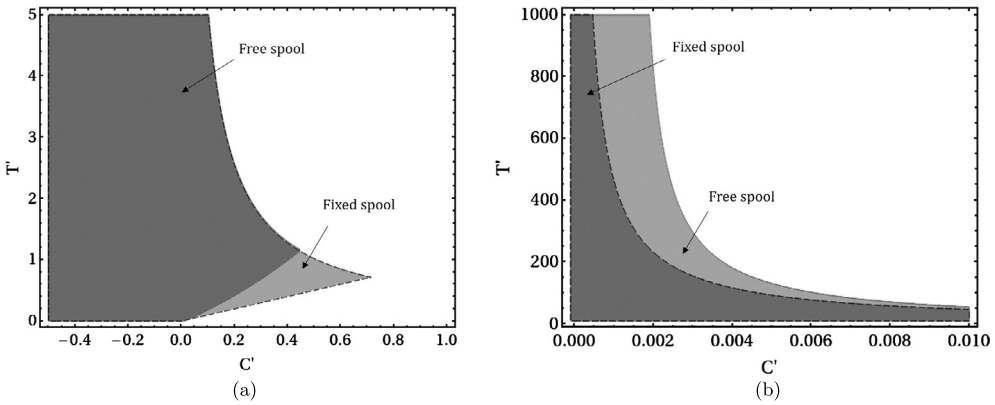

Fig. 13. (a) Direct comparison of stable operating range of G_{model} and F_{model} with same system configuration, (b) Comparison of stable operating range at larger value of T'.

in order to show the differences between G_{model} and F_{model} clearer, Fig. 13a presents the direct comparison of stable operating range of the two models.

As shown in Fig. 13a, fixed speed model shows narrowed stable operating range as T' increases (equivalent to closing the downstream valve). Normally, the compressor downstream valve is operating near its choke conditions, thus its characteristic curve is so steep (with the value of T' generally larger than 3) that $Cond1$ dominates the system stability as shown in Fig. 12a. For the variable speed model, the overall stable region is further restricted by $Cond3$ at smaller values of T' (smaller than 3) where the compressor system seldom operates, as shown in Fig. 12b. Within the normal operating range, two models show similar stable ranges. Therefore, even though the order of the systems is elevated after introducing the rotor dynamics, dominant effect of Cond1 still holds true in the normal operating conditions. The stabilizing effect by speed variation becomes clear with the value of T' increased as shown in Fig. 13b, which presents the stable operating regions at the range of T' up to 1000.

$$Cond1 : \begin{cases} \frac{1}{\overline{B}T'} - BC' \ (G_{model}) \\ \frac{1}{\overline{B}T'} - \overline{B}C' - A_s\overline{B}(\overline{B}\Gamma_d' + \overline{\Phi}_c\Gamma_c') \ (F_{model}) \end{cases} \tag{11}$$

$$Cond4 = Cond1 * Cond2 - Cond3 \tag{12}$$

Within normal operating range (the value of T' higher than 3), the values of $Cond2$ and $Cond3$ are always positive as shown in Fig. 12. Therefore, to evaluate the speed variation contribution to the surge limit, a new parameter can be defined from the expression of $Cond1$ (F_{model}) as $\mathrm{SVC} = \overline{B}\Gamma_d' + \overline{\Phi}_c\Gamma_c'$. If SVC > 0, the value of $Cond1$ (F_{model}) is negative at the stable boundary defined by $Cond1$ (G_{model}) $= 0$ according to Equation (11), which thereby makes $Cond4$ violated (negative) according to Equation (12), thus

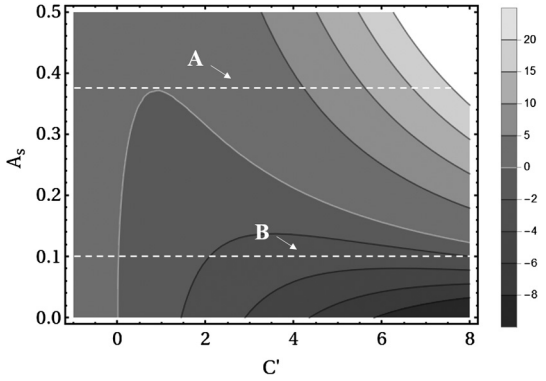

Fig. 14. Contour map of $Cond4$ with respect to A_s and C' ($T' = 400$, SVC < 0).

speed variation narrows the stable operating range with the rotor dynamics considered. On the other hand, if SVC < 0, which is the more common case, $Cond1$ (F_{model}) is always satisfied at the boundary, therefore, it is no longer $Cond1$ (F_{model}), but $Cond4$ that determines the stabilizing effect of the variable speed system.

Due to the dependence of SVC on the system parameters (especially parameter B) and turbine characteristic (Γ_d'), it is possible to design a compressor system and control logic with smallest possible value of SVC to avoid the side effects brought by speed variation when SVC > 0. While negative SVC may help to stabilize the compressor system, which has inspired some works on active control of compressor system based on high-frequency spool speed control during surge inception phase.

To further analyze the stabilizing effects of speed variation in the negative range of SVC, the contour map of $Cond4(F_{model})$ is calculated with respect to A_s and C' as shown in Fig. 14. The solid white curve represents critical stable operating conditions, above which the system stays stable while the lower region indicates unstable operation. Generally, the shaft with a smaller moment of inertia tends to be more stable, especially for the value of A_s larger than 0.38 (indicated by line A) that the stable operating range even extends to positive slope regions ($C' > 0$). For the range of A_s between line A and B, a switching region between stability and instability appears and extends as A_s decreases. The classic instability-growth pattern can be expected below line B. For the tested case in this paper, the value of A_s is around 0.04 which is located below line B. Therefore, the system would always go into surge at a critical point around $C' = 0$. With the rotor dynamics are considered, it is possible to extend the stable operating range significantly by reducing shaft moment of inertia through better structural design and material advancement.

5. Conclusion

System dynamic simulations have been conducted in combination with the experimental results to investigate the role of speed variation on surge characteristics and behaviors of compression systems. Moreover, results from the perturbation method are discussed to highlight the effect of speed variation on the surge limit. Several conclusions are drawn as follows.

1. The analytical model of a free-spool compression system is established. Simulation results show better agreement with the experimental data compared to the fixed-spool simulation. The mechanism of the prolonged surge cycle is presented. During surge, the rotational speed decreases to the degree that the operating point moves far away enough from the surge line that can endure the potential energy of the compressed air stored in the downstream plenum, then quasi-steady acceleration process (quiet period) follows which is responsible for the dramatically prolonged time of surge cycle.
2. The inconsistency of surge dynamics between different rotational speeds and design cases are explained. The different relative position of the compressor surge line and the averaged deceleration line (valve characteristic) is believed to be the primary cause of this inconsistency. Different shape and location of the compressor surge line are influenced by the design features, pressure ratio and flow capacity. As a result, surge behaves differently.
3. The perturbation method is applied to analyze the stability of the free-spool compression system. Based on it, speed variation contribution factor SVC is proposed to evaluate the effects of speed variation on the compressor stable operating range. For negative values of SVC, speed variation has negative effects on the system stability, while systems with positive SVC exhibit possibility of stability enhancement by reducing the rotational inertia.

Declaration of competing interest

The authors declare that they have no known competing financial interests or personal relationships that could have appeared to influence the work reported in this paper.

Acknowledgement

This research was supported by the National Science and Technology Major Project of China (2017-II-0004-0016), the National Natural Science Foundation of China (Grant No. 51876097).

Appendix A

The derivative of system parameter is expressed as a function of U and T_p:

$$\frac{dB}{dt} = \frac{B}{U}\frac{dU}{dt} - \frac{B}{2a}\sqrt{\frac{kR}{T_p}}\frac{dT_p}{dt}$$

if isentropic compression and expansion process is assumed in the plenum, the second term can be expressed by

$$\frac{dT_p}{dt} = \frac{k-1}{k}\frac{T_p}{P_p}\frac{dP_p}{dt}$$

combined with Equation (4) and Equation (9), dB/dt can be derived:

$$\frac{dB}{dt} = -\frac{1}{2\Psi_p}\frac{k-1}{k}(\Phi_c - \Phi_t) + A_s B^2(\Gamma_d - \Gamma_c)$$

Appendix B

The coefficient matrix A of linearized governing equations is obtained from Equation (10):

$$\begin{bmatrix} \overline{B}C' + A_s\overline{B}\Gamma_c'\overline{\Phi}_c & -\overline{B} & -A_s\overline{B}\Gamma_d'\overline{\Phi}_c \\ \frac{1}{B} + 2A_s\overline{B}\Gamma_d'\overline{\Psi}_p & -\frac{1}{\overline{B}T'} & -2A_s\overline{B}\Gamma_d'\overline{\Psi}_p \\ -\frac{k-1}{2k}\frac{1}{\overline{\Psi}_p} - A_s\overline{B}^2\Gamma_c' & -\frac{k-1}{2k}\frac{1}{\overline{\Psi}_p} & A_s\overline{B}^2\Gamma_d' \end{bmatrix}$$

Eigenvalues of the corresponding matrix A are calculated by setting the characteristic polynomial $||A - \lambda I||$ to be zero. The Routh–Hurwitz criterion is utilized to decide the system stability without computing the roots, thus four conditions are derived for the variable speed model F_{model}:

$$Cond1: \quad (\frac{1}{\overline{B}T'} - \overline{B}C') - A_s\overline{B}(\overline{B}\Gamma_d' + \overline{\Phi}_c\Gamma_c')$$

$$\begin{aligned} Cond2: \quad & (1 - \frac{C'}{T'}) + A\overline{B}^2\Gamma_d'(2\overline{\Psi}_p + \overline{B}C') \\ & - \frac{A\overline{B}\Gamma_d'}{2k\overline{\Psi}_pT'}(2k\overline{\Psi}_p(1+T') + kT'\overline{\Phi}_c - T'(2\overline{\Psi}_p + \overline{\Phi}_c)) \\ & + \frac{A\Gamma_c'\overline{\Phi}_c}{T'} \end{aligned}$$

$$\begin{aligned} Cond3: \quad & -A\Gamma_d'(2A\overline{B}^4\overline{\Psi}_p(\Gamma_d' - \Gamma_c') \\ & - \frac{\overline{B}^2}{kT'}(T'(A\overline{\Phi}_c(k-1)(\Gamma_c' - \Gamma_d') - 1) \\ & + C'(k - T' + kT')) + \frac{\overline{\Phi}_c(k-1)(1+T')}{2k\overline{\Psi}_pT'}) \end{aligned}$$

$$Cond4: \quad Cond1 * Cond2 - Cond3$$

The two conditions of the fixed speed model are obtained by setting A_s to zero:

$$Cond1: \quad \frac{1}{\overline{B}T'} - \overline{B}C'$$

$$Cond2: \quad 1 - \frac{C'}{T'}$$

System stable operation is realized when all the conditions are positive for each model.

References

[1] J.B. Erskine, N. Hensman, Vibration induced by pump instability and surging, in: Vibrations and Noise in Pump, Fan, and Compressor Installations, 1975, pp. 87–98.

[2] K. Brun, S. Simons, R. Kurz, E. Munari, M. Morini, M. Pinelli, Measurement and prediction of centrifugal compressor axial forces during surge—part I: surge force measurements, J. Eng. Gas Turbines Power 140 (1) (2017), https://doi.org/10.1115/1.4037662.

[3] E. Munari, M. Morini, M. Pinelli, K. Brun, S. Simons, R. Kurz, A new index to evaluate the potential damage of a surge event: the surge severity coefficient, J. Eng. Gas Turbines Power 141 (3) (2018), https://doi.org/10.1115/1.4041255.

[4] E. Munari, G. D'Elia, M. Morini, M. Pinelli, P.R. Spina, Stall and surge in wet compression: test rig development and experimental results, J. Eng. Gas Turbines Power 141 (7) (2019), https://doi.org/10.1115/1.4042474.

[5] Z. Sun, W. Zou, X. Zheng, Instability detection of centrifugal compressors by means of acoustic measurements, Aerosp. Sci. Technol. 82–83 (2018) 628–635, https://doi.org/10.1016/j.ast.2018.09.006.

[6] A. Ghenaiet, S. Khalfallah, Assessment of some stall-onset criteria for centrifugal compressors, Aerosp. Sci. Technol. 88 (2019) 193–207, https://doi.org/10.1016/j.ast.2018.12.039.

[7] X. He, X. Zheng, Roles and mechanisms of casing treatment on different scales of flow instability in high pressure ratio centrifugal compressors, Aerosp. Sci. Technol. 84 (2019) 734–746, https://doi.org/10.1016/j.ast.2018.10.015.

[8] H. Pearson, T. Bowmer, Surging of axial compressors, Aeronaut. Q. 1 (3) (1949) 195–210, https://doi.org/10.1017/s0001925900000159.

[9] H.W. Emmons, Compressor surge and stall propagation, Trans. Am. Soc. Mech. Eng. 77 (1955) 455–469.

[10] E.M. Greitzer, Surge and rotating stall in axial flow compressors—part II: experimental results and comparison with theory, J. Eng. Power 98 (2) (1976) 199–211, https://doi.org/10.1115/1.3446139.

[11] K.E. Hansen, P. Jorgensen, P.S. Larsen, Experimental and theoretical study of surge in a small centrifugal compressor, J. Fluids Eng. 103 (3) (1981) 391–395, https://doi.org/10.1115/1.3240796.

[12] J.E. Pinsley, G.R. Guenette, A.H. Epstein, E.M. Greitzer, Active stabilization of centrifugal compressor surge, J. Turbomach. 113 (4) (1991) 723–732, https://doi.org/10.1115/1.2929139.

[13] M. van de Wal, F. Willems, B. de Jager, Selection of actuators and sensors for surge control, J. Propuls. Power 18 (1) (2002) 84–92, https://doi.org/10.2514/2.5901.

[14] I.J. Day, Axial compressor performance during surge, J. Propuls. Power 10 (3) (1994) 329–336, https://doi.org/10.2514/3.23760.

[15] J.T. Gravdahl, O. Egeland, Compressor Surge and Stall: An Introduction, Springer London, 1999.

[16] E.M. Greitzer, Surge and rotating stall in axial flow compressors—part I: theoretical compression system model, J. Eng. Power 98 (2) (1976) 190–198, https://doi.org/10.1115/1.3446138.

[17] F.K. Moore, A theory of rotating stall of multistage axial compressors—part I: small disturbances, J. Eng. Gas Turbines Power 106 (2) (1984) 313–320, https://doi.org/10.1115/1.3239565.

[18] F.K. Moore, A theory of rotating stall of multistage axial compressors—part II: finite disturbances, J. Eng. Gas Turbines Power 106 (2) (1984) 321–326, https://doi.org/10.1115/1.3239566.

[19] C.A. Mansoux, D.L. Gysling, J.D. Setiawan, J.D. Paduano, Distributed nonlinear modeling and stability analysis of axial compressor stall and surge, in: Proceedings of 1994 American Control Conference, IEEE, 1994.

[20] M. Righi, V. Pachidis, L. Könözsy, L. Pawsey, Three-dimensional through-flow modelling of axial flow compressor rotating stall and surge, Aerosp. Sci. Technol. 78 (2018) 271–279, https://doi.org/10.1016/j.ast.2018.04.021.

[21] M. Zhang, X. Zheng, Q. Huang, Z. Sun, A novel one-dimensional-three-dimensional coupled method to predict surge boundary of centrifugal compressors, J. Eng. Gas Turbines Power 141 (7) (2019), https://doi.org/10.1115/1.4042419.

[22] D.A. Fink, N.A. Cumpsty, E.M. Greitzer, Surge dynamics in a free-spool centrifugal compressor system, J. Turbomach. 114 (2) (1992) 321–332, https://doi.org/10.1115/1.2929146.

[23] A. Abrassi, A. Traverso, L. Ferrari, Turbocharger-based hybrid systems: modeling and validation of a free spool subject to compressor surge, in: Volume 3: Coal, Biomass, and Alternative Fuels; Cycle Innovations; Electric Power; Industrial and Cogeneration; Organic Rankine Cycle Power Systems, American Society of Mechanical Engineers, 2018.

[24] J.T. Gravdahl, F. Willems, B. de Jager, O. Egeland, Modeling of surge in free-spool centrifugal compressors: experimental validation, J. Propuls. Power 20 (5) (2004) 849–857, https://doi.org/10.2514/1.10052.

[25] X. Zheng, Z. Sun, T. Kawakubo, H. Tamaki, Experimental investigation of surge and stall in a turbocharger centrifugal compressor with a vaned diffuser, Exp. Therm. Fluid Sci. 82 (2017) 493–506, https://doi.org/10.1016/j.expthermflusci.2016.11.036.

[26] S.G. Koff, E.M. Greitzer, Stalled flow performance for axial compressors—part I: axisymmetric characteristic, in: Volume 1: Turbomachinery, American Society of Mechanical Engineers, 1984.

[27] O. Leufven, L. Eriksson, Surge and choke capable compressor model, IFAC Proc. Vol. 44 (1) (2011) 10653–10658, https://doi.org/10.3182/20110828-6-it-1002.00694.

[28] Kulite pressure transducer handbook, Kulite.

[29] X. He, X. Zheng, Flow instability evolution in high pressure ratio centrifugal compressor with vaned diffuser, Exp. Therm. Fluid Sci. 98 (2018) 719–730, https://doi.org/10.1016/j.expthermflusci.2018.06.023.